Earth and Planetary Science Letters 476 (2017) 79–86

Contents lists available at ScienceDirect

Earth and Planetary Science Letters

www.elsevier.com/locate/epsl

Magmatic architecture within a rift segment: Articulate axial magma storage at Erta Ale volcano, Ethiopia

Wenbin Xu [a,*], Eleonora Rivalta [b], Xing Li [a]

[a] Department of Land Surveying and Geo-informatics, The Hong Kong Polytechnic University, Kowloon, Hong Kong, China
[b] GFZ German Research Centre for Geosciences, Telegrafenberg, 14473 Potsdam, Germany

ARTICLE INFO

Article history:
Received 21 April 2017
Received in revised form 29 July 2017
Accepted 30 July 2017
Available online xxxx
Editor: T.A. Mather

Keywords:
slow spreading ridge
Erta Ale volcano
lava lake
InSAR
magma plumbing system

ABSTRACT

Understanding the magmatic systems beneath rift volcanoes provides insights into the deeper processes associated with rift architecture and development. At the slow spreading Erta Ale segment (Afar, Ethiopia) transition from continental rifting to seafloor spreading is ongoing on land. A lava lake has been documented since the twentieth century at the summit of the Erta Ale volcano and acts as an indicator of the pressure of its magma reservoir. However, the structure of the plumbing system of the volcano feeding such persistent active lava lake and the mechanisms controlling the architecture of magma storage remain unclear. Here, we combine high-resolution satellite optical imagery and radar interferometry (InSAR) to infer the shape, location and orientation of the conduits feeding the 2017 Erta Ale eruption. We show that the lava lake was rooted in a vertical dike-shaped reservoir that had been inflating prior to the eruption. The magma was subsequently transferred into a shallower feeder dike. We also find a shallow, horizontal magma lens elongated along axis inflating beneath the volcano during the later period of the eruption. Edifice stress modeling suggests the hydraulically connected system of horizontal and vertical thin magmatic bodies able to open and close are arranged spatially according to stresses induced by loading and unloading due to topographic changes. Our combined approach may provide new constraints on the organization of magma plumbing systems beneath volcanoes in continental and marine settings.

1. Introduction

The Erta Ale volcanic segment in Afar, Ethiopia, is a ~120 km long continuous range comprising several Quaternary shield complexes cut by normal faults in the Danakil depression, part of the Africa–Arabia extensional plate boundary. It represents the northernmost segment in the Afar depression, which lies at the triple junction between the southern Red Sea, the main Ethiopian rift and the Gulf of Aden (Manighetti et al., 1998; Beyene and Abdelsalam, 2005). It is a region where the transition from continental rifting to seafloor spreading is ongoing on land (Bosworth et al., 2005; Hayward and Ebinger, 1996), thus representing a key region to investigate the early developmental stage of Mid Ocean Ridges.

One debated issue is how the magma plumbing system transforms during the transition from continental to oceanic rifting. Analysis of the pre- and co-eruptive crustal deformation associated with the 2008 fissure eruption at Alu-Dalafilla in the Erta Ale Range revealed that the feeder dike propagated vertically from the side edge of a shallow reservoir at 1 km depth, shaped as an axial horizontal magma lens (Field et al., 2012; Pagli et al., 2012). This highlighted a similarity with magma storage geometry at fast-spreading Mid-Ocean Ridges (MORs), where shallow axial magma lenses are often imaged as seismic reflectors (e.g. Singh et al., 2006). This association is puzzling since the Erta Ale Ridge is slow-spreading at ~12 mm yr^{-1}. At slow-spreading mid-ocean ridges in contrast magma chambers are generally deeper and approximately axisymmetric, and inject dikes laterally along the ridge axes (Singh et al., 2006; Schlindwein and Schmid, 2016). Other Afar segments, where axisymmetric melt accumulation zones at mid-crustal to shallow depths have fed laterally propagating dikes, are geometrically consistent with these models (Wright et al., 2006; Grandin et al., 2010; Nobile et al., 2012; Hamiel and Baer, 2016). The Alu Dalafilla example and earlier studies on the slow-spreading Reykjanes Ridge, where an axial magma lens was inferred at 2.5 km beneath the sea floor (Sinha et al., 1998; Navin et al., 1998), highlight that spreading rate cannot be the only control on the morphology of adolescent or mature spreading ridges.

Another question to answer is whether elongated, axial magma chambers may be common to the entire Erta Ale range, and what controls such apparently anomalous geometry and shallow depth.

* Corresponding author.
E-mail address: wenbin.xu@polyu.edu.hk (W. Xu).

http://dx.doi.org/10.1016/j.epsl.2017.07.051
0012-821X/

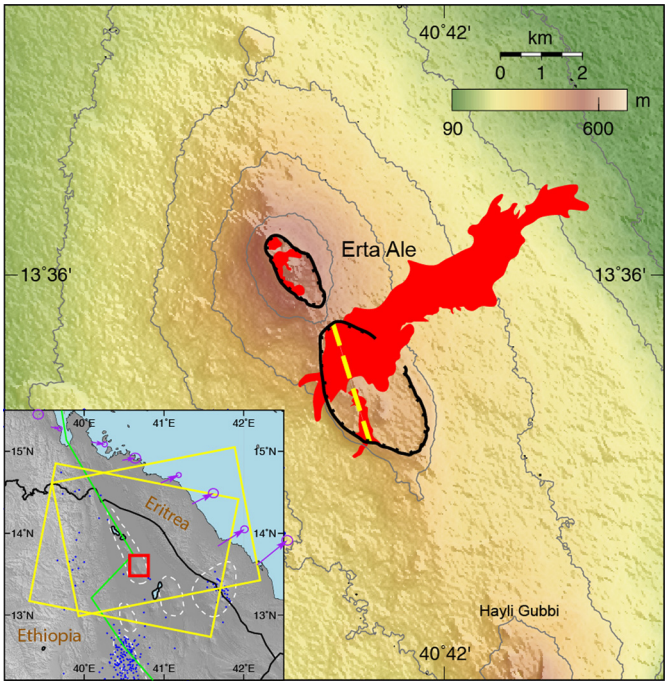

Fig. 1. Location of the Erta Ale volcano. The coverage of the new lavas is shown in red. The eruptive fissure in shown in yellow dashed line. The crater's rim is marked by ticked black lines. The contour has an interval of 100 m. Inset: Blue dots represent two decades of earthquakes from the National Earthquake Information Center catalog. Yellow boxes outline ascending and descending orbit SAR frames. The red rectangle outlines the study area. Green line marks the plate boundary in the region (Bird, 2003), purple arrows show GPS velocities with 95% confidence ellipses in a Eurasia-fixed reference frame (ArRajehi et al., 2010). (For interpretation of the colors in this figure, the reader is referred to the web version of this article.)

Pagli et al. (2012) proposed that the lack of hydrothermal circulation or an excess heat advection in the Erta Ale Range may be responsible for the observed inconsistency with models on mid-oceanic reservoirs, which would predict a depth of ~4 km for the Alu Dalafilla magma chamber.

The recent (January 2017) eruption at Erta Ale volcano offers an opportunity to look into the plumbing system of one of the most active volcanoes within the Danakil depression (Fig. 1). Erta Ale volcano has an open vent system with the existence of a persistent active lava lake at its summit. The lava lake responds dynamically to pressure change in the magma reservoir at depth (Patrick et al., 2015, 2016). Recent volcanic activity at Erta Ale includes an overflow event of the lava lake in the southern pit crater, which occurred in 2010 (Field et al., 2012), but no crustal deformation studies were available that can unveil its shallow plumbing system. Here, we use satellite optical imagery and interferometric synthetic aperture radar (InSAR) data to unveil the course of the eruption. We document how the lava flows progressed, investigate the pre- and co-eruptive magma accumulation and transfer in the shallow magma plumbing system of Erta Ale and discuss the findings in the light of models of shape and depth of magma storage and its tectonic and magmatic controls. We further model the orientation of principal stresses to explore the influence of topographic changes on the arrangement of shallow magmatic bodies.

2. Co-eruptive high-resolution satellite optical images

High-resolution optical images from multiple satellites with different spatial resolutions acquired before and during the 2017 Erta Ale eruption provide detailed information about the volcanic activity and the evolution of new lava flows (Table S1). A pre-eruption Landsat-8 image (15 m) acquired seven days prior to the first lava lake overflowing (17 Jan. 2017) shows that a large area at the summit of the Erta Ale volcano was covered by old lavas (Fig. 2a). The lava lake within the southern pit was clearly visible suggesting that pressure was high in the magma chamber. No earthquakes were detected teleseismically nor by the local array which can locate $M_L > 3$ events (Atalay Ayele, personal communication). A Sentinel-2 (S2) satellite image (20 m) acquired on 19 January captures the first phase of the 2017 eruption (Fig. 2b). It shows that the lava lake was overflowing and sending fresh lavas toward south and southwest. The lava traveled about 1 km along the southwest caldera rim from the lava lake and did not flow outside the caldera (Fig. 2b). The estimated area of the newly deposited lava was about 0.34 km^2 between 10 and 19 January (see Fig. S1 for a summary of the lava coverage vs. time).

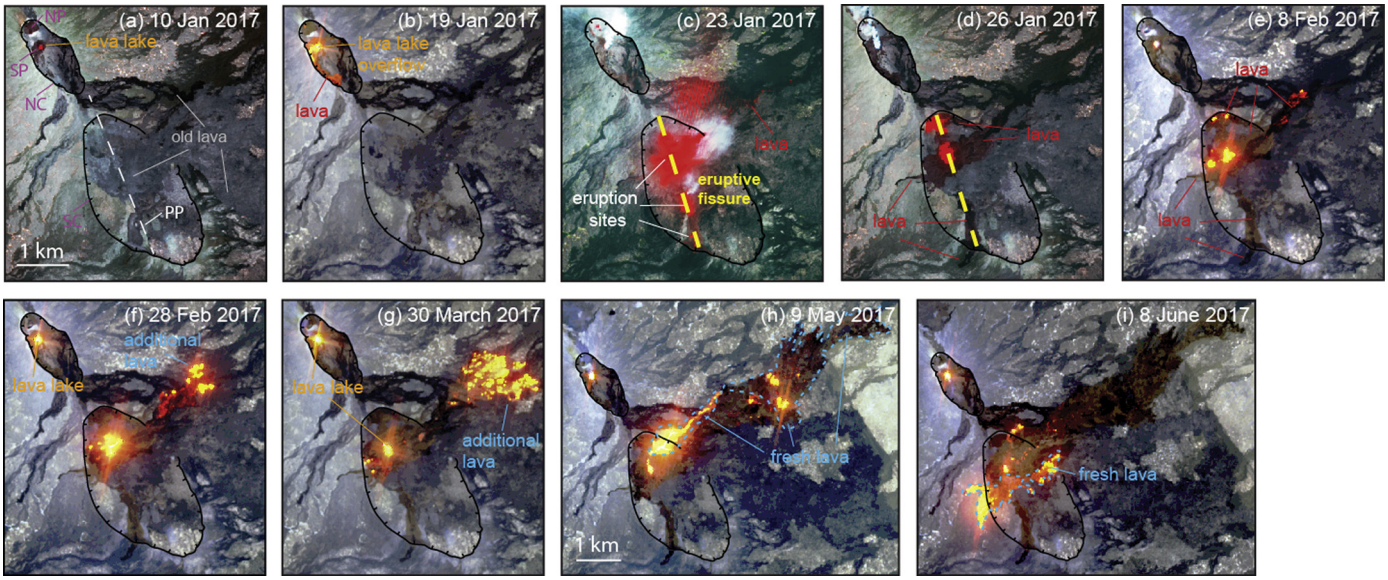

Fig. 2. A series of satellite optical imagery close-ups of the summit area of Erta Ale showing the 2017 eruption. (a) A pre-eruption image. (b) Lava overflowing from the southern pit. (c–i) Eruption occurring within the southern crater with lava flow outside the rim from the eruptive fissure. Black ticked lines mark the crater's rim. The image in (a and d) is from Landsat-8 (bands 6, 4, 3 and 8), (c) EO-1 ALI (bands 9, 6, 5 and 1), and (b, e–i) Sentinel-2 (bands 12, 11, and 8A). Note the different scale in (h) and (i). NC, northern caldera; SC, southern caldera; NP, northern pit; SP, southern pit; PP, pre-existing pathway.

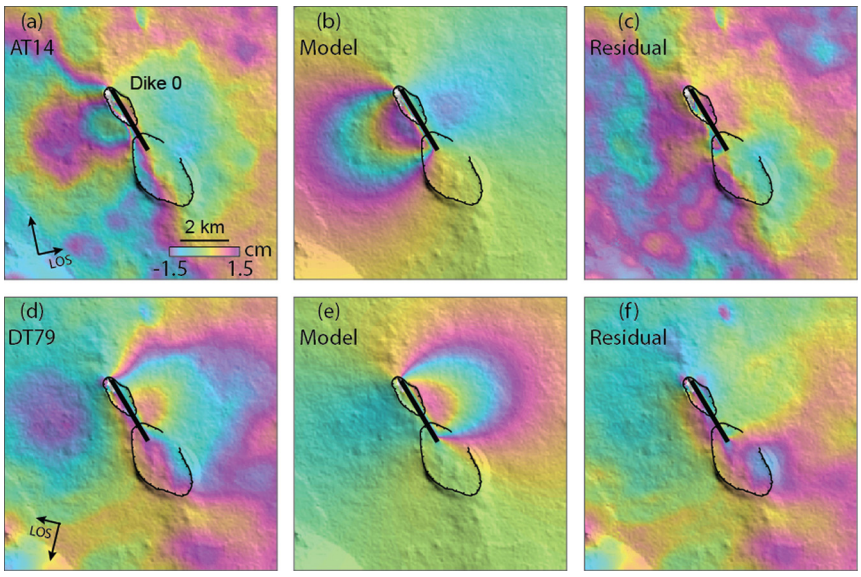

Fig. 3. Interferograms spanning one year prior to the 2017 Erta Ale eruption and the modeling result. From left to right: Observed (first column) data, (second column) model predictions, (third column) residuals. The interferograms were unwrapped and then rewrapped with each fringe representing 3 cm displacement in line-of-sight (LOS) direction. Black line marks the modeled inflation dike 0.

The second phase of eruption was observed in an Earth Observing-1 (EO-1) image (10 m resolution) on 23 January (Fig. 2c). At least three fissure eruption sites were clearly visible within the southern caldera. A branch of lava flow was seen on the eastern flank of the volcano reaching a distance of about 3 km from the eruptive fissure. The lava lake of the south pit stopped overflowing and the north pit seemed to have grown larger possibly due to collapse of the pit wall. On 26 January, a Sentinel-2 image shows that the volcanic activity mainly focused on two northern eruption sites within the southern caldera and steam was seen from both pits within the northern caldera (Fig. 2d). About 2.69 km^2 new lavas were ejected from the fissures within the southern caldera till 26 January 2017.

Between 26 January and 8 February 2017, the two lava lakes within the northern caldera remained at a high level while lava continuously flowed out from two eruption sites within the southern caldera, adding 0.15 km^2 of new lava coverage (Fig. 2e). On 28 February 2017 the eruption condensed to one eruption site within the southern caldera; the lava lake of the south pit remained high (Fig. 2f). Additional lava flow was seen on the eastern flank of the volcano enlarging the lava coverage to about 0.4 km^2. The total surface covered with lava was estimated to be about 3.58 km^2 by 28 February 2017. A second lava lake was clearly seen within the southern caldera depositing additional 0.51 km^2 lava on the NE flank as observed on 30 Mar 2017 (Fig. 2g). The thermal signal gap between the lava lake and the active flow field suggest that the lava flowed towards the front through a tube. The total surface covered by new lava was estimated to be about 4.09 km^2.

The volcanic activity within the southern caldera was very active. The newly formed lava lake sent a large amount of lavas toward its northeastern direction (Fig. 2h) covering an additional area of about 3.9 km^2. Further activity in June shows that the lavas were mainly deposited within the southern caldera as well as flowed over the caldera in southwesterly direction (Fig. 2i).

3. Data processing and deformation modeling

We generate pre-, co-, and post-eruptive interferograms from the European Space Agency's (ESA) Sentinel-1 images in both ascending and descending orbits (Table S2). The Sentinel-1 data were acquired in the Terrain Observation by Progressive Scan (TOPS) mode. Very accurate coregistration is needed to mitigate azimuth phase ramps across TOPS interferograms (Xu et al., 2016). We adapt a two-step coregistration approach implemented in the GAMMA software to do the coregistration between the master and slave images. We use the intensity cross-correlation method followed by the spectral diversity method to ensure that the coregistration accuracy reaches an accuracy of ~1/1000 pixel. After successful coregistration, we follow the standard two-pass differential InSAR method in the data processing. We use the 1 arc second Shuttle Radar Topography Mission (SRTM) digital elevation model (DEM) for topographic corrections (Farr et al., 2007). We apply multilook operation of 10×2 pixels in range and azimuth direction and unwrap the filtered interferograms with a minimum cost flow method (Chen and Zebker, 2001). The topography-dependent atmospheric effects and remaining orbital errors seen on the interferograms are jointly estimated and removed (Xu et al., 2014).

To retrieve near field deformation, we calculate the range offsets using search patches of 100×20 pixels (Michel et al., 1999). To maintain a similar pixel spacing with the InSAR measurement, the range offsets are estimated for every 10×2 (range and azimuth, respectively) pixels. The SRTM DEM is used to remove geometrical offsets seen in the rugged terrain areas. Finally, a median filter (8×8) is used to further reduce the noises of the calculated offsets.

Before performing the inversion, we subsample our data points using the quadtree method (Jónsson et al., 2002) and weight the data according to their variance. We then search for the source parameters that minimize the weighted root-mean-square misfit between the data and the model's predictions. We estimate the best fitting model parameters by using a Monte Carlo-type simulated annealing algorithm (Cervelli et al., 2001), followed by a gradient-based method. We use rectangular dislocations (Okada, 1985) to model the data, assuming a homogeneous and isotropic elastic half-space without considering the effect of topography. We find that including the topography in the modeling (Williams and Wadge, 2000) broadens the predicted deformation but the effects are secondary. As suggested by the deformation pattern (see section 4 below), we set the dislocations to be either vertical (hereafter referred to as "dikes") or horizontal (hereafter referred to as "sills") and use the offset measurements to fix their location and search for their optimal geometry and uniform opening. We apply least squares inversion to determine the finite sill opening that fits

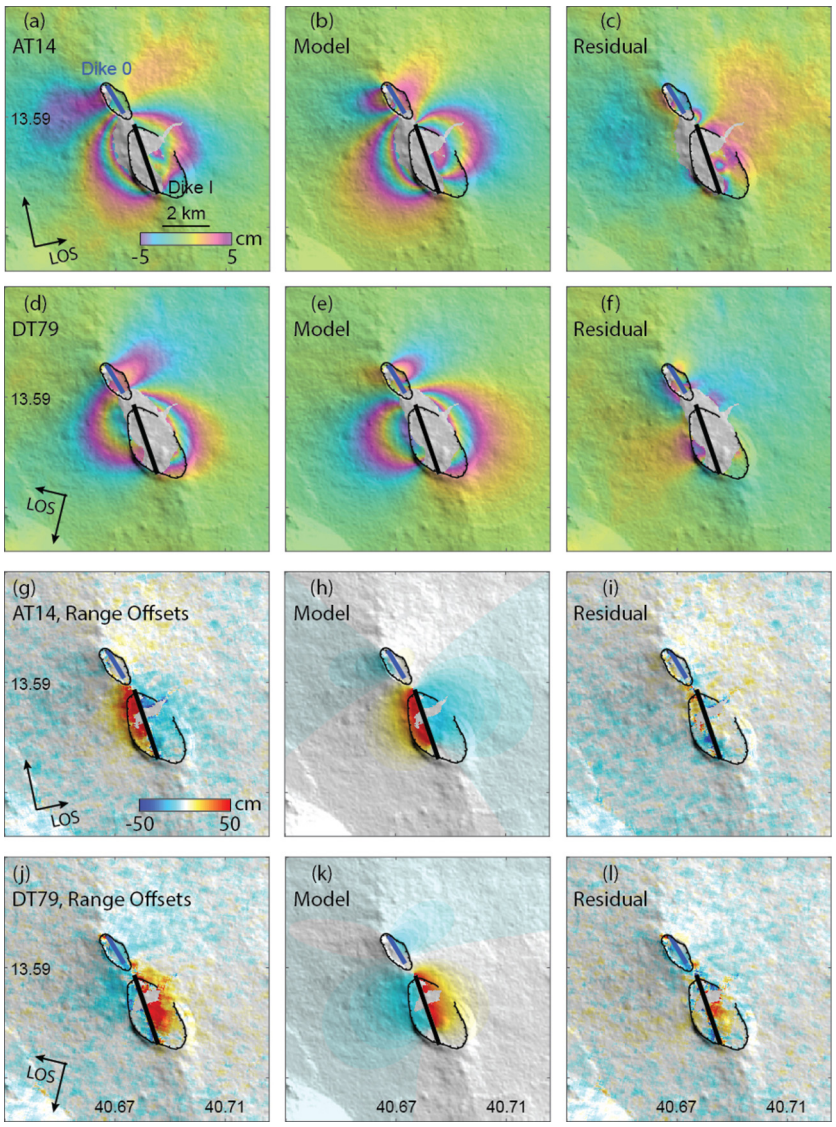

Fig. 4. The early co-eruptive InSAR data (4 January 2017–4 February 2017) of the 2017 Erta Ale eruption and the modeling result. From left to right: Observed (first column) data, (second column) model predictions, (third column) residuals. The interferograms (first two rows) were unwrapped and then rewrapped with each fringe representing 10 cm displacement in LOS direction. The SAR-image range offsets (last two rows) showing the LOS ground displacements. Note the different LOS directions for the (first and third rows) ascending and (second and last rows) descending orbit data. Blue line marks the modeled deflation dike 0, and black line the inflation dike I. (For interpretation of the references to color in this figure, the reader is referred to the web version of this article.)

best with the InSAR data set. The uncertainty of source parameters is estimated using the so-called randomize-then-optimize method (Bardsley et al., 2014; Xu et al., 2016). In this method, we perturb the original data by adding random noise and generate multiple data realizations (here 500 realizations). From each of these data realizations, we estimate the source parameters; the distribution of the estimated values reflects their uncertainty.

4. Observed deformation and modeling results

The three interferograms span different periods of the eruptive activity at Erta Ale volcano. The first Sentinel-1 interferogram spans a one-year period of ground deformation prior to the eruption; the second interferogram covers the main phase of the eruption including the lava lake overflowing in the northern caldera and the fissure eruption within the southern caldera; The third interferogram covers the late stage of the eruption.

4.1. The pre-eruptive deformation: 17 January 2016–11 January 2017

Individual interferograms spanning one month-long time periods prior to the eruption show no appreciable ground deformation except during the five days prior to the eruption (Fig. S2). The accumulative interferograms spanning approximately one year from both ascending and descending orbits exhibit ~3 cm of line-of-sight (LOS) deformation on each side of Erta Ale volcano. The elongate, approximately antisymmetric deformation pattern in interferograms from both orbits suggests opening of a precursory vertical dike (dike 0) (Fig. 3). Inversion results show that the dike-shaped magma accumulation structure reached shallow depth beneath the surface and had an average opening of $\sim 13^{3}_{-2}$ cm and a volume change of $1.8^{0.1}_{-0.04} \times 10^{6}$ m^3.

4.2. The early co-eruptive deformation: 4 January 2017–4 February 2017

For the early co-eruptive phase, we consider interferograms covering the time period of lava lake overflowing (northern

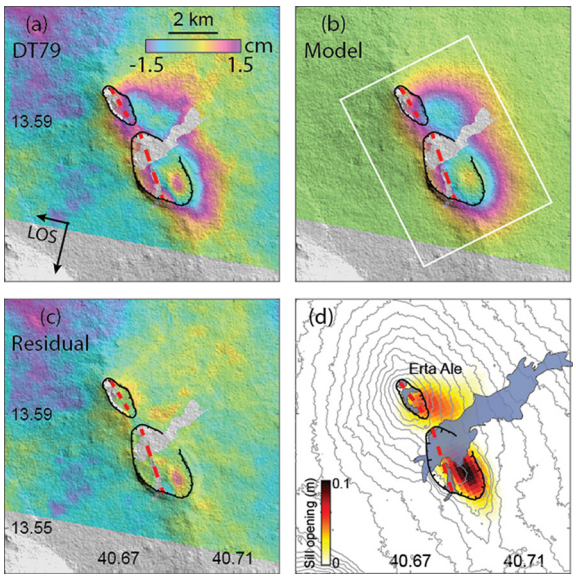

Fig. 5. The late co-eruptive InSAR data (28 January 2017–5 March 2017) of the 2017 Erta Ale eruption and the modeling result. (a) Observed data. The red dashed line mark the modeled dikes in Fig. 4. (b) Model prediction. The white rectangle outlines the modeled sill. (c) Residual. The interferograms were unwrapped and then rewrapped with each fringe representing 3 cm displacement in LOS direction. (d) Plan view of the co-eruptive distributed sill inflation overlaid by topographic contours (35 m interval) and lava flow (gray). (For interpretation of the colors in this figure, the reader is referred to the web version of this article.)

caldera) and the fissure eruption (southern caldera) (Fig. 4). The interferograms show that most deformation in the wider area occurred during the time period of the fissure eruption in the southern caldera, implying hydraulic linkage in the plumbing system below the two calderas. InSAR coherence is low within the southern caldera, mainly due to the large deformation gradients in this area or lava coverage, which exceeds the resolvability of InSAR. However, range offsets show up to 50 cm LOS displacements within the southern caldera.

The deformation pattern to the south suggests again a dike intrusion, while in the north the opposite fringe pattern is suggestive of a closing of part of Dike 0. For the modeling, we adopt the location, depth, strike and dip of the pre-eruptive Dike 0 and use information from the satellite optical imagery (Fig. 2) and range offsets (Fig. 4) to constrain the location, geometry and strike of the opening and closing dislocations and estimate their parameters. We find that the Dike 0 has an average closure of $\sim 40^{15}_{26}$ cm and a volume decrease of $\sim 1.8^{0.11}_{-0.18} \times 10^6$ m^3. The estimated average opening and volume of Dike I is $\sim 120^{18}_{-13}$ cm and $1.9^{0.13}_{-0.05} \times 10^6$ m^3, respectively. Thus, in spite of the large difference in average opening of the dike sources, the volume increase in Dike 0 during the pre-eruptive period matches within errors both the volume decrease of Dike 0 and the volume increase of Dike I during the early co-eruptive phase. However, we were not able to comment on the lava lake levels change during the different phases. The unmolded residuals are likely due to the model simplifications and atmospheric artifacts.

4.3. The late co-eruptive deformation (phase II): 28 January 2017–5 March 2017

During this time period, the eruptive activity has significantly decreased. The activity condensed to a cone where lava continuously flows out to north-northeast direction causing loss of interferometric coherence. One descending interferogram shows a broad, volcano-wide uplifting zone beneath both calderas (Fig. 5). A concentrated fringe pattern is limited to the southern caldera's floor showing strong uplifting signal of about 4 cm in LOS, while a lower deformation signal of about 2 cm in LOS exists southeast of the northern caldera. The best-fitting model for the largely symmetric deformation pattern highlighted by the interferogram suggests a sill-shaped source located at $\sim 1.3^{0.74}_{-0.34}$ km that inflates by up to 10^7_{-5} cm and exhibits a volume increase of $4.8^{0.29}_{-0.2} \times 10^6$ m^3. This depth value likely indicates the depth of the top of the sill, as crustal deformation is only sensitive to the top of pressurized magma chambers and is insensitive to the sides and bottom of the chamber (Yun et al., 2006). No obvious volcano-wide ground deformation is seen from InSAR data between 5 March and 9 June 2017 (Fig. S3).

5. Numerical stress model

Magma-filled cracks tend to align with σ_1 and σ_2, the most compressive and intermediate stress axes, respectively (Anderson, 1951); thus, modeling the stress state of a volcano may help understanding the observed spatial configuration of the volcano plumbing system and vice versa. Previous studies have highlighted that surface loading stresses such as those due to the presence of a volcanic edifice may dominate the local stress field (e.g. Pinel and Jaupart, 2003, 2004, Karlstrom et al., 2009), induce a rotation of the principal stress axes and bend the pathways of propagating dikes (e.g. Watanabe et al., 2002). Corbi et al. (2015, 2016) modeled numerically and experimentally the decompression generated by the presence of a caldera and found that a sill is expected below the caldera floor and vertical dikes laterally to it, below the rim.

We follow this line of research and construct a model of the stress state of Erta Ale, determined by edifice loading and the presence of a caldera. Although deeper density contrasts may exist that may influence the crustal state of stress, the short-wavelength signals we detect are caused by shallow sources, the focus of our study. We first calculate the surface loading due to the development of the Erta Ale Range topography as observed today. We use analytical 2D (plane-strain) expressions for a distribution of forces on the surface (e,g, Jaeger, 1969), that we constrain by taking a $\sim$300 km long topographic profile perpendicular to the axis of the Erta Ale Range through the northern caldera (a portion of which is visible in Fig. 6a, data are from GeoMapApp). We assume that the original height of the Earth's surface was at 250 m (this parameter does not have a large influence because it impacts mostly the trace of the stress tensor and not the deviatoric stresses), so that all locations on the profile higher and lower than 250 m are treated as causing loading and unloading, respectively. Next we include the contribution exerted by caldera formation, following Corbi et al. (2015). We reconstruct the summit of Erta Ale prior to the collapse (Fig. 6b) and superpose loading forces equal to $-\rho g \Delta h$, where ρ is host rock edifice density (we use 2700 kg m^{-3}) and Δh is the height difference between the reconstructed and the observed volcano profile. We increase Δh by 10% to account for a locally smaller density just below the caldera floor. We neglect tectonic extensional stresses due to the high rate of intrusions at Erta Ale that relieve tectonic stress (Oppenheimer and Francis, 1998; Barnie et al., 2016) and the shallow depths considered here. Finally, we consider that background edifice stresses evolve slowly owing to a number of inelastic, stress-homogenizing processes such as seismicity, that releases shear stresses, and diking, that increases σ_3 until all principal stresses become similar (Chadwick and Dieterich, 1995; Corbi et al., 2015). We evaluate the fraction of background stress retained in the shallow crust. We explore values in the range 0–50% (bracketed by values used previously, see Corbi et al. (2015)) and find that 10% results in principal stress orientations matching best with the observed dike and sill orientations.

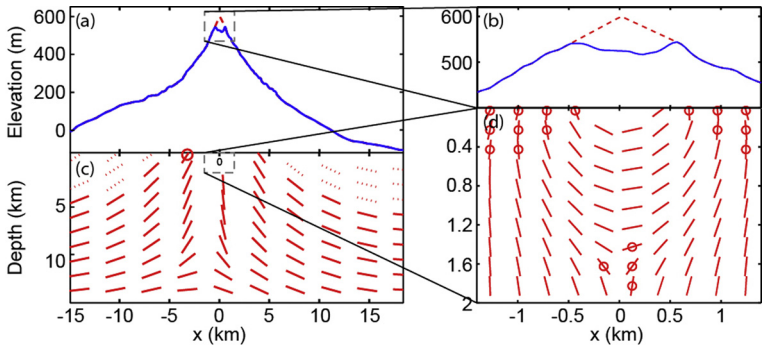

Fig. 6. Analytical model of the stress state of Erta Ale. a) Topography of the volcano perpendicular to the Range axis and through the northern caldera. In red, correction to estimate the pre-collapse topographic profile. b) Zoom-in of (a). c) Principal stress orientations resulting from 10% of the original topographic stresses plus unloading stresses. Red segments indicate the expected orientation of magma-filled dikes and sills: they describe the orientation of σ_1. If a red circle is present, σ_3 is out-of-plane, so that dikes are expected to propagate lying on the page plane. Dashed segments indicate the direction of σ_2 if σ_1 is out-of-plane. d) Zoom in of (c) for the rock volume around the magma plumbing structures. (For interpretation of the colors in this figure, the reader is referred to the web version of this article.)

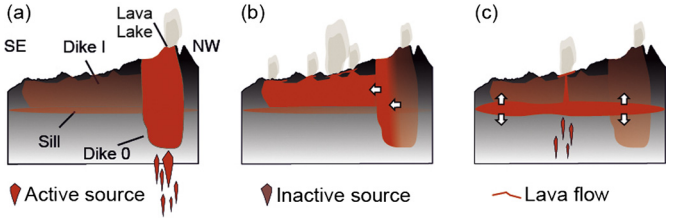

Fig. 7. Schematic cross section (NW–SE) across Erta Ale volcano showing the inferred magma systems, viewing from NE side of the volcano. (a) The lava lake overflowing and lava flow on the floor within the northern caldera. (b) The early eruption involving a fissure eruption within the southern caldera. (c) The late eruption involving a sill inflation. The figure is not to scale and is not reflecting the fluctuation of lava lake.

With this set of assumptions, at crustal scale, the resulting stress pattern is dominated by the loading of the elongated Erta Ale volcanic range (Fig. 6c) with the modeled magma trajectories converging from the sides into the base of the volcano; in contrast, at more local scale the caldera unloading dominates, inducing a horizontal σ_1 and a vertical σ_3 in the rock volume above ~1.4 km depth just below the caldera (Fig. 6d). This state of stress favors shallow horizontal magma lenses forming below the calderas. Just to the sides of the rock volume below the caldera, σ_1 becomes vertical and σ_3 horizontal, favoring vertical dikes below the rim and just within the caldera.

6. Discussion

The dynamics of magma transfer in the shallow plumbing system at Erta Ale as revealed by our analysis of InSAR data raises several questions on how the different pieces of the plumbing system interact, whether they may be long-lived, on the role played by hydraulic connectivity and pressure variations, and how to reconcile the overall geometry with the slow-spreading nature of the tectonic setting.

Inversion of pre-eruption InSAR data suggests that the summit lava lake has been connected to a conduit shaped as a dike (Dike 0), although InSAR data do not have enough resolution to detect deep sources of deformation and thus the root of the dike and its relationship to the deeper magma source (Fig. 7). Examples of vertical, relatively flat conduits shrinking during eruption exist (Costa et al., 2007; Hautmann et al., 2009; Patrick et al., 2015, 2016; Nikkhoo et al., 2017), but Dike 0 reaches an unusually shallow depth. Previous studies show that a dike-shaped deformation source of similar location, orientation and volume has undergone intermittent cycles of inflation and deflation in the last 15 yrs (Barnie et al., 2016). Thus, Dike 0 may be a relatively permanent structure of the plumbing system. This suggests that either Dike 0 is thermally stable thanks to magma convection and heat advection through the entire system, or that a thermally stable, smaller-sized conduit breaks regularly into a dike of similar orientation and shape. Oppenheimer and Francis (1998) argued that convection in the summit lava lake limits the buoyancy of magma by removing heat so to favor intrusions and endogenous growth of the edifice rather than eruptions.

The eruptive fissure (Dike I) is about 12° oblique to the regional trend. A pre-eruption optical image shows that Dike I might have occupied the pathway of previous feeder dikes (Fig. 2a). This pre-existing structure may explain the mismatch in orientation (e.g. Ruch et al., 2016), but other reasons may also play a role, especially considering that the long-term orientation of magma pathways also requires an explanation. Gravitational stresses (Dahm, 2000; Maccaferri et al., 2011; Sigmundsson et al., 2015) or other stress gradients (Dahm, 2000) may drive dikes oblique to the most extensional stress direction. Another reason may be that edifice stresses may differ slightly from regional stresses. Modeling results show that the Dike 0 is rooted at depth while Dike I is entirely shallow. The shallow local stress field is probably decoupled from the regional stress field (Xu and Jónsson, 2014).

The sill-shaped axial body detected at $\sim 1.3^{0.74}_{-0.34}$ km confirms that shallow horizontal elongated magma lenses are not unique to Alu Dalafilla volcano but may be common in the Erta Ale Range. The uplift signal has two distinct maxima located at the southern caldera and just off the center of the northern caldera, thus appearing correlated with the morphology of the volcanic edifice. A similar loose correlation of maximum sill opening with grabens on the surface of Alu and especially South East of Dalafilla emerges by comparing the inversion of InSAR data with satellite imagery (Global Volcanism Program, 2013). Our 2D stress model is inadequate to test such correlation, since the structure of the horsts and grabens of which the edifices are composed is strongly 3D (Barberi and Varet, 1970).

A link between depth, shape and orientation of magma storage and edifice construction or destruction has been suggested by previous numerical modeling studies (Pinel and Jaupart, 2000; Dahm, 2000; Maccaferri et al., 2015; Corbi et al., 2015). At Erta Ale, a similar surface loading model is consistent with the complex orientation and the depth of magma storage. In particular, stresses arising from the existence of a double caldera explain the tendency of the system to develop an axial magma lens bordered by a vertical dike. The architecture of magma storage and crustal accretion in other equally slow-spreading east African locations, which have the more typical morphology with a broad axial valley, is more often characterized by magma lenses located at depths ranging from a few km to about 10 km, and by vertical dikes propagating lat-

erally along the rift axis away from them (Wright et al., 2012). As shown by Maccaferri et al. (2014), the surface loading model predicts that the depth of magma lenses below topographic depressions scales with the width of the depression. Wider grabens in extensional regimes are associated with stress fields favoring deeper horizontal magma lenses, with the depth resulting from the competition between depth of the depression and tectonic extension. Above such lenses, the stress field favors vertical dikes propagating laterally along the rift axis (Maccaferri et al., 2014). Thus, the surface loading model is consistent with the architecture of magma plumbing both at Erta Ale (a ridge with small axial calderas, prescribing shallow horizontal lens) and with other Afar locations with a wider graben. In this model supply rate and heat flow controls how long-lived the magma lenses are, but not the depth of magma storage, that is controlled, beside surface loads and degree of tectonic extension, by other forces such as magma buoyancy and rock resistance to fracture (Pinel and Jaupart, 2000).

Mechanisms and parameters thought to control the architecture of axial magma lenses at MORs include spreading rate, magma and heat supply rate (e.g. in relation to the presence of a plume), and cooling rate due to hydrothermal circulation. Ridge morphology is thought to be controlled by these many factors in interplay with extensional tectonics, rather than being itself a controlling factor. A correlation between topography and depth of magma lenses has been previously suggested also in the context of fast-spreading Mid Ocean Ridges. Carbotte et al. (2006) analyzed the along-axis structure of the Juan de Fuca Ridge. They found that axial grabens are associated to shallow crustal sills, and that the axial grabens disappear where the magma lens also disappears. Based on this correlation, Carbotte et al. (2006) concluded that the topography profile is magmatically, rather than tectonically controlled as previously thought, thus suggesting a control in the opposite way as what we suggest here. In our interpretation the similarity between the Erta Ale Ridge plumbing system to that of the Reykjanes ridge or fast-spreading MORs may descend from the similarity of their topographic profiles: a ridge with a small graben at its top (Sinha et al., 1998; Navin et al., 1998). Quantitative dedicated tests are required before discussing whether the surface loading model may help understanding better magma storage at MORs.

7. Conclusions

The combined use of satellite optical images and InSAR observations to study the 2017 Erta Ale volcanic activity enabled us to analyze the shallow magma plumbing system of the Erta Ale volcano. A series of satellite optical images from multiple platforms capture the surface changes with a high spatial and temporal resolution. It shows that the eruption started with lava lake overflowing resulting in fresh lava flows in the northern caldera. Later during the eruption, the activity decreased in the northern caldera but shifted to the southern caldera where a dike opened up and sent voluminous lavas within the caldera and to the eastern flank of the volcano. InSAR observations and modeling results show that the shallow magma plumbing system of the Erta Ale volcano is complex involving the interaction of varyingly oriented melt lenses. A dike-shaped reservoir connecting the deep source with the lava lake at the summit is hydraulically connected with an elongated shallow dike that enable magma to propagate horizontally to fed the fissure eruption in the southern caldera. The side edge of a shallow horizontal reservoir connects with the elongated dike. Taken together with previous findings on Alu Dalafilla volcanoes (Pagli et al., 2012), our new observations provide further evidence for the existence of semi-permanent axial magma lenses along the length of the Erta Ale magmatic segment. The architecture of magma lenses at the Erta Ale Range and in other magmatic rift systems may be shaped by stresses induced top-down by surface loading or unloading.

Acknowledgements

We would like to thank Editor Tamsin Mather, Cindy Ebinger and one anonymous reviewer for critical comments and suggestions. We thank Sigurjón Jónsson for early review of the manuscript. Sentinel-1 SAR images were downloaded from the Sentinel-1 Scientific Data Hub (https://scihub.copernicus.eu). Several figures were prepared by using Generic Mapping Tools software and GeoMapApp. The research was supported by the Hong Kong Polytechnic University startup grant (1-ZE6R). The MATLAB code used to model the edifice stresses is available by contacting the authors.

Appendix A. Supplementary material

Supplementary material related to this article can be found online at http://dx.doi.org/10.1016/j.epsl.2017.07.051.

References

Anderson, E., 1951. The Dynamics of Faulting and Dyke Formation with Applications to Britain. Oliver and Boyd, Edinburgh.

ArRajehi, A., et al., 2010. Geodetic constraints on present-day motion of the Arabian Plate: implications for Red Sea and Gulf of Aden rifting. Tectonics 29, TC3011. http://dx.doi.org/10.1029/2009TC002482.

Barberi, F., Varet, J., 1970. The Erta Ale volcanic range (Danakil Depression, Northern Afar, Ethiopia). Bull. Volcanol. 34 (4), 848–917.

Bardsley, J.M., Solonen, A., Haario, H., Laine, M., 2014. Randomize-then-optimize: a method for sampling from posterior distributions in nonlinear inverse problems. SIAM J. Sci. Comput. 36, A1895–A1910.

Barnie, T.D., Oppenheimer, C., Pagli, C., 2016. Does the lava lake of Erta Ale volcano respond to regional magmatic and tectonic events? An investigation using Earth observation data. In: Wright, T.J., Ayele, A., Ferguson, D.J., Kidane, T., Vye-Brown, C. (Eds.), Magmatic Rifting and Active Volcanism, Geol. Soc. (Lond.) Spec. Publ. 420. http://dx.doi.org/10.1144/SP420.15.

Beyene, A., Abdelsalam, M.G., 2005. Tectonics of the Afar depression: a review and synthesis. J. Afr. Earth Sci. 41 (1), 41–59. http://dx.doi.org/10.1016/j.jafrearsci.2005.03.003.

Bird, P., 2003. An updated digital model of plate boundaries. Geochem. Geophys. Geosyst. 4, 1027. http://dx.doi.org/10.1029/2001GC000252.

Bosworth, W., Huchon, P., McClay, K., 2005. The Red sea and Gulf of Aden basins. J. Afr. Earth Sci. 43 (1), 334–378. http://dx.doi.org/10.1016/j.jafrearsci.2005.07.020.

Carbotte, S.M., Detrick, R.S., Harding, A., Canales, J.P., Babcock, J., Kent, G., Van, A.E., Nedimovic, M., Diebold, J., 2006. Rift topography linked to magmatism at the intermediate spreading Juan de Fuca Ridge. Geology 34, 209–212. http://dx.doi.org/10.1130/g21969.1.

Cervelli, P., Murray, M.H., Segall, P., Aoki, Y., Kato, T., 2001. Estimating source parameters from deformation data, with an application to the March 1997 earthquake swarm off the Izu Peninsula, Japan. J. Geophys. Res. 106 (B6), 11217–11238. http://dx.doi.org/10.1029/2000JB900399.

Chadwick Jr, W.W., Dieterich, J.H., 1995. Mechanical modeling of circumferential and radial dike intrusion on Galapagos volcanoes. J. Volcanol. Geotherm. Res. 66, 37–52. http://dx.doi.org/10.1016/0377-0273(94)00060-T.

Chen, C.W., Zebker, H.A., 2001. Two-dimensional phase unwrapping with use of statistical models for cost functions in nonlinear optimization. J. Opt. Soc. Am. A 18, 338–351. http://dx.doi.org/10.1364/JOSAA.18.000338.

Corbi, F., Rivalta, E., Pinel, V., Maccaferri, F., Bagnardi, M., Acocella, V., 2015. How caldera collapse shapes the shallow emplacement and transfer of magma in active volcanoes. Earth Planet. Sci. Lett. 431, 287–293. http://dx.doi.org/10.1016/j.epsl.2015.09.028.

Corbi, F., Rivalta, E., Pinel, V., Maccaferri, F., Acocella, V., 2016. Understanding the link between circumferential dikes and eruptive fissures around calderas based on numerical and analog models. Geophys. Res. Lett. 43, 6212–6219. http://dx.doi.org/10.1002/2016GL068721.

Costa, A., Melnik, O., Sparks, R.S.J., 2007. Controls of conduit geometry and wallrock elasticity on lava dome eruptions. Earth Planet. Sci. Lett. 260 (1–2), 137–151. http://dx.doi.org/10.1016/j.epsl.2007.05.024.

Dahm, T., 2000. Numerical simulations of the propagation path and the arrest of fluid-filled fractures in the Earth. Geophys. J. Int. 141 (3), 623–638. http://dx.doi.org/10.1002/2016GL069820.

Farr, T.G., et al., 2007. The shuttle radar topography mission. Rev. Geophys. 45, RG2004. http://dx.doi.org/10.1029/2005RG000183.

Field, L., Barnie, T., Blundy, J., Brooker, R.A., Keir, D., Lewi, E., Saunders, K., 2012. Integrated field, satellite and petrological observations of the November 2010 eruption of Erta Ale. Bull. Volcanol. 74 (10), 2251–2271. http://dx.doi.org/10.1007/s00445-012-0660-7.

Global Volcanism Program, 2013. Alu-Dalafilla (221060) in Volcanoes of the World, v. 4.5.5. Venzke, E. (ed.). Smithsonian Institution. Downloaded 19 Apr 2017 http://dx.doi.org/10.5479/si.GVP.VOTW4-2013 http://volcano.si.edu/volcano.cfm?vn=221060.

Grandin, R., Socquet, A., Jacques, E., Mazzoni, N., de Chabalier, J.B., King, G.C.P., 2010. Sequence of rifting in Afar, Manda-Hararo rift, Ethiopia, 2005–2009: time–space evolution and interactions between dikes from interferometric synthetic aperture radar and static stress change modeling. J. Geophys. Res., Solid Earth 121.115 (B10). http://dx.doi.org/10.1029/2009JB000815.

Hamiel, Y., Baer, G., 2016. Crustal deformation associated with the 2011 eruption of the Nabro volcano, Eritrea. Tectonophysics 691, 257–262. http://dx.doi.org/10.1016/j.tecto.2016.10.013.

Hautmann, S., Gottsmann, J., Sparks, R.S.J., Costa, A., Melnik, O., Voight, B., 2009. Modelling ground deformation caused by oscillating overpressure in a dyke conduit at Soufrière Hills Volcano, Montserrat. Tectonophysics 471 (1–2), 87–95. http://dx.doi.org/10.1016/j.tecto.2008.10.021.

Hayward, N.J., Ebinger, C.J., 1996. Variations in the along-axis segmentation of the Afar Rift System. Tectonics 15 (2), 244–257. http://dx.doi.org/10.1029/95TC02292.

Jaeger, J.C., 1969. Elasticity, Fracture, and Flow, 3rd edition. Methuen, London. 268 pp.

Jónsson, S., Zebker, H., Segall, P., Amelung, F., 2002. Fault slip distribution of the 1999 Mw 7.1 Hector Mine, California, earthquake, estimated from satellite radar and GPS measurements. Bull. Seismol. Soc. Am. 92 (4), 1377–1389. http://dx.doi.org/10.1785/0120000922.

Karlstrom, L., Dufek, J., Manga, M., 2009. Organization of volcanic plumbing through magmatic lensing by magma chambers and volcanic loads. J. Geophys. Res. 114, B10204. http://dx.doi.org/10.1029/2009JB006339.

Maccaferri, F., Bonafede, M., Rivalta, E., 2011. A quantitative study of the mechanisms governing dike propagation, dike arrest and sill formation. J. Volcanol. Geotherm. Res. 208 (1–2), 39–50. http://dx.doi.org/10.1016/j.jvolgeores.2011.09.001.

Maccaferri, F., Rivalta, E., Keir, D., Acocella, V., 2014. Off-rift volcanism in rift zones determined by crustal unloading. Nat. Geosci. 7, 297–300. http://dx.doi.org/10.1038/ngeo2110.

Maccaferri, F., Acocella, V., Rivalta, E., 2015. How the differential load induced by normal fault scarps controls the distribution of monogenic volcanism. Geophys. Res. Lett. 42 (18), 7507–7512.

Manighetti, I., Tapponnier, P., Gillot, P.Y., Jacques, E., Courtillot, V., Armijo, R., Ruegg, J.C., King, G., 1998. Propagation of rifting along the Arabia–Somalia Plate Boundary: Into Afar. J. Geophys. Res. 103 (B3), 4947–4974. http://dx.doi.org/10.1029/97JB02758.

Michel, R., Avouac, J.P., Taboury, J., 1999. Measuring ground displacements from SAR amplitude images: application to the Landers earthquake. Geophys. Res. Lett. 26 (7), 875–878. http://dx.doi.org/10.1029/1999GL900138.

Navin, D.A., Peirce, C., Sinha, M.C., 1998. The RAMESSES experiment—II. Evidence for accumulated melt beneath a slow spreading ridge from wide-angle refraction and multichannel reflection seismic profiles. Geophys. J. Int. 135, 746–772.

Nikkhoo, M., Walter, T.R., Lundgren, P.R., Prats-Iraola, P., 2017. Compound dislocation models (CDMs) for volcano deformation analyses. Geophys. J. Int. 208 (2), 877–894. http://dx.doi.org/10.1093/gji/ggw427.

Nobile, A., Pagli, C., Keir, D., Wright, T.J., Ayele, A., Ruch, J., Acocella, V., 2012. Dike-fault interaction during the 2004 Dallol Intrusion at the northern edge of the Erta Ale Ridge (Afar, Ethiopia). Geophys. Res. Lett. 39 (19). http://dx.doi.org/10.1029/2012GL053152.

Okada, Y., 1985. Surface deformation due to shear and tensile faults in a half-space. Bull. Seismol. Soc. Am. 75 (4), 1135–1154.

Oppenheimer, C., Francis, P., 1998. Implications of longeval lava lakes for geomorphological and plutonic processes at Erta 'Ale volcano, Afar. J. Volcanol. Geotherm. Res. 80 (1), 101–111. http://dx.doi.org/10.1016/S0377-0273(97)00041-3.

Pagli, C., Wright, T.J., Ebinger, C.J., Yun, S.H., Cann, J.R., Barnie, T., Ayele, A., 2012. Shallow axial magma chamber at the slow-spreading Erta Ale Ridge. Nat. Geosci. 5 (4), 284–288. http://dx.doi.org/10.1038/ngeo1414.

Patrick, M.R., Anderson, K.R., Poland, M.P., Orr, T.R., Swanson, D.A., 2015. Lava lake level as a gauge of magma reservoir pressure and eruptive hazard. Geology 43 (9), 831–834. http://dx.doi.org/10.1016/j.epsl.2015.10.052.

Patrick, M.R., Orr, T., Sutton, A.J., Lev, E., Thelen, W., Fee, D., 2016. Shallowly driven fluctuations in lava lake outgassing (gas pistoning), Kīlauea Volcano. Earth Planet. Sci. Lett. 433, 326–338. http://dx.doi.org/10.1130/G36896.1.

Pinel, V., Jaupart, C., 2000. The effect of edifice load on magma ascent beneath a volcano. Philos. Trans. R. Soc. London, Ser. A 358, 1515–1532.

Pinel, V., Jaupart, C., 2003. Magma chamber behavior beneath a volcanic edifice. J. Geophys. Res. 108 (B2), 2072. http://dx.doi.org/10.1029/2002JB001751.

Pinel, V., Jaupart, C., 2004. Magma storage and horizontal dyke injection beneath a volcanic edifice. Earth Planet. Sci. Lett. 221 (1–4), 245–262.

Ruch, J., Wang, T., Xu, W., Hensch, M., Jónsson, S., 2016. Oblique rift opening revealed by reoccurring magma injection in central Iceland. Nat. Commun. 7, 12352.

Schlindwein, V., Schmid, F., 2016. Mid-ocean-ridge seismicity reveals extreme types of ocean lithosphere. Nature 535, 267–279. http://dx.doi.org/10.1038/nature18277.

Sigmundsson, F., et al., 2015. Segmented lateral dyke growth in a rifting event at Bárðarbunga volcanic system, Iceland. Nature 517, 191–195. http://dx.doi.org/10.1038/nature14111.

Singh, S.C., et al., 2006. Discovery of a magma chamber and faults beneath a Mid-Atlantic Ridge hydrothermal field. Nature 442, 1029–1032. http://dx.doi.org/10.1038/nature05105.

Sinha, M.C., Constable, S.C., Peirce, C., White, A., Heinson, G., MacGregor, L.M., Navin, D.A., 1998. Magmatic processes at slow spreading ridges: implications of the RAMESSES experiment at 57°45′N on the Mid-Atlantic Ridge. Geophys. J. Int. 135, 731–745.

Watanabe, T., Masuyama, T., Nagaoka, K., Tahara, T., 2002. Analog experiments on magma-filled cracks: competition between external stresses and internal pressure. Earth Planets Space 54, 1247–1261. http://dx.doi.org/10.1186/BF03352453.

Williams, C.A., Wadge, G., 2000. An accurate and efficient method for including the effects of topography in three-dimensional elastic models of ground deformation with applications to radar interferometry. J. Geophys. Res. 105, 8103–8120. http://dx.doi.org/10.1029/1999JB900307.

Wright, T.J., Ebinger, C., Biggs, J., Ayele, A., Yirgu, G., Keir, D., Stork, A., 2006. Magma-maintained rift segmentation at continental rupture in the 2005 Afar dyking episode. Nature 442, 291–294. http://dx.doi.org/10.1038/nature04978.

Wright, T.J., Sigmundsson, F., Pagli, C., Belachew, M., Hamling, I.J., Brandsdóttir, B., Keir, D., Pedersen, R., Ayele, A., Ebinger, C., Einarsson, P., Lewi, E., Calais, E., 2012. Geophysical constraints on the dynamics of spreading centres from rifting episodes on land. Nat. Geosci. 5 (4), 242–250. http://dx.doi.org/10.1038/ngeo1428.

Xu, B., Li, Z.W., Wang, Q.J., Jiang, M., Zhu, J.J., Ding, X.L., 2014. A refined strategy for removing composite errors of SAR interferogram. IEEE Geosci. Remote Sens. Lett. 11 (1), 143–147. http://dx.doi.org/10.1109/LGRS.2013.2250903.

Xu, W., Jónsson, S., 2014. The 2007–8 volcanic eruption on Jebel at Tair island (Red Sea) observed by satellite radar and optical images. Bull. Volcanol. 76, 795. http://dx.doi.org/10.1007/s00445-014-0795-9.

Xu, W., Jónsson, S., Corbi, F., Rivalta, E., 2016. Graben formation and dike arrest during the 2009 Harrat Lunayyir dike intrusion in Saudi Arabia: insights from InSAR, stress calculations and analog experiments. J. Geophys. Res., Solid Earth 121, 2837–2851. http://dx.doi.org/10.1002/2015JB012505.

Yun, S., Segall, P., Zebker, H., 2006. Constraints on magma chamber geometry at Sierra Negra Volcano, Galápagos Islands, based on InSAR observations. J. Volcanol. Geotherm. Res. 150, 232–243. http://dx.doi.org/10.1016/j.jvolgeores.2005.07.009.